Flow, Turbulence and Combustion
https://doi.org/10.1007/s10494-024-00593-9

RESEARCH

Turbulence Structure and Mixing in Strongly Stable Couette Flows over Thermally Heterogeneous Surfaces: Effect of Heterogeneity Orientation

Dmitrii Mironov[1] **· Peter Sullivan**[2]

Received: 26 June 2024 / Accepted: 8 October 2024

Abstract

Direct numerical simulations (DNS) of plane Couette flows over thermally heterogeneous surfaces at bulk Reynolds number $Re = 10^4$ and bulk Richardson number $Ri = 0.25$ are performed. The focus of the present study (that extends previous work by the authors) is the effect of surface heterogeneity orientation on boundary-layer structure. The temperature of the upper and lower walls is either homogeneous or varies sinusoidally, where the temperature-wave crests are either normal or parallel to the mean flow (HETx and HETy cases, respectively). Importantly, the horizontal-mean surface temperature is the same in all simulations. The stratification is strong enough to quench turbulence over a homogeneous surface, but turbulence survives over heterogeneous surfaces. In all heterogeneous cases, both molecular diffusion and turbulence transfer momentum down the gradient of mean velocity. The total (turbulent plus diffusive) heat flux is down-gradient, but quasi-organized eddy motions generated by the surface thermal heterogeneity induce heat transfer up the gradient of the mean temperature. Comparative analysis of HETx and HETy cases shows that the configuration with the spanwise heterogeneity is more turbulent and more efficient in transporting momentum and heat vertically than its counterpart with the streamwise heterogeneity. Vertical profiles of mean fields and turbulence moments differ considerably between the HETx and HETy cases, e.g., the streamwise heat flux differs not only in magnitude but also in sign. A close examination of the second-order turbulence moments, vertical-velocity and temperature skewness, and the flow eddy structure helps explain the observed differences between the HETx and HETy cases. The implications of our DNS findings for modelling turbulence in stably-stratified environmental and industrial flows with surface heterogeneity are discussed.

Keywords Strongly stable boundary layer · Surface thermal heterogeneity · Turbulence · Couette flow · Direct numerical simulation

✉ Dmitrii Mironov
dmitrii.mironov@dwd.de

Peter Sullivan
pps@ucar.edu

[1] Deutscher Wettedienst, 63067 Offenbach am Main, Germany

[2] National Center for Atmospheric Research, Boulder, CO 80307, USA

Published online: 20 November 2024

1 Introduction

Representation of stably stratified boundary-layer (SBL) turbulence is of paramount importance in many industrial and environmental applications. In numerical weather prediction and climate studies, for example, model errors, associated with relatively weak and often intermittent turbulence and low mixing intensity that are characteristic of the SBL, are substantial (Holtslag et al. 2013). It is still largely unclear how to cure the trouble. Many features of stably-stratified boundary-layer turbulence are poorly understood (see, e.g., Mahrt 2014, for discussion of atmospheric SBLs). One particularly challenging problem is the strongly stable boundary-layer flow over a thermally heterogeneous surface. In the present study, direct numerical simulation (DNS) is used to examine the effect of surface thermal heterogeneity on the mean and turbulence structure and mixing intensity in strongly stable boundary-layer flows. More specifically, we analyze the effect of the orientation of the surface heterogeneity patterns relative to the mean velocity on the boundary-layer structure. The present study extends previous studies by the authors (Mironov and Sullivan 2016, 2023) where several aspects of the SBL over heterogeneous surfaces have been addressed.

Mironov and Sullivan (2016, hereafter MS16) used large-eddy simulation (LES) to gain insight into the structure and transport properties of the atmospheric SBL over thermally homogeneous and thermally heterogeneous surfaces. A comparative analysis of mean fields and second-moment budgets in homogeneous and heterogeneous SBLs was performed. A physically sound explanation of the enhanced mixing in the heterogeneous SBL was suggested, and possible ways to account for the heterogeneity effects in coarse-resolution models of atmospheric flows were discussed. It should be stressed that the results of MS16 are pertinent to weakly-to-moderately stable boundary layers, where turbulence is continuous and rather vigorous over both homogeneous and heterogeneous surfaces.

Mironov and Sullivan (2023, hereafter MS23) performed direct numerical simulation to analyze the structure of strongly stable SBL with surface thermal heterogeneity (the idea to use LES was abandoned since LESs of strongly stable flows heavily depend on the sub-grid scale parameterizations and are very uncertain). An idealized plane Couette flow configuration is used as a proxy for real-world SBLs. The temperature of the upper and lower walls is either homogeneous or varied sinusoidally in the streamwise direction, but the horizontal-mean surface temperature is the same in both homogeneous and heterogeneous simulations. Turbulence cannot survive over a homogeneous surface because of the strong buoyancy stratification. However, turbulence survives over heterogeneous surfaces. Examination of momentum and heat fluxes shows that both molecular and turbulent fluxes of momentum are down-gradient, whereas the turbulent contribution to the heat flux is up the gradient of mean temperature. Analysis of the flow structure and of the skewness of velocity and temperature fields suggests that the counter-gradient turbulent heat transfer is caused by quasi-organized vortical motions similar to quasi-organized motions (e.g., plumes and rolls) encountered in convective boundary layers. Those eddy motions cause counter-gradient heat transfer, although the overall stratification remains stable and the total (diffusive plus turbulent) heat flux is down-gradient. The DNS findings of MS23 corroborate the LES findings of MS16, emphasizing the key role of the temperature variance in setting the structure and mixing intensity in stably-stratified flows over heterogeneous surfaces. Both LES and DNS results indicate the importance of third-order transport of the temperature variance.

The analysis of MS23 is focused on the Couette flow configuration where the crests of the surface temperature waves are normal to the mean flow. The present study extends the study of MS23 by analyzing the effect of the orientation of the surface heterogeneity patterns on the mean and turbulence structure and transport properties of plane Couette flows. We compare results of simulations where the temperature-wave crests are normal to the mean flow (as in MS23, hereafter referred to as HETx cases) and parallel to the mean flow (HETy cases). We examine mean fields, second-order turbulence moments (variances and fluxes), and the vertical-velocity and temperature skewness. We also perform a visualization study of the flow eddy structure.

The goal of the present study is not to simulate specific industrial or environmental flows, e.g., atmospheric or oceanic SBLs. Instead, we focus on physical processes at work in strongly stratified boundary-layer flows over thermally heterogeneous surfaces, viz., on the effect of the orientation of the surface heterogeneity patterns on the structure and transport properties of turbulence. For this purpose, a plane Couette flow set-up is used (a physical analog of our numerical configuration, a channel-like laboratory tank of infinite band type, is briefly discussed in MS23). The plane Couette flow configuration has often been used to explore various aspects of neutral and stratified turbulence (see, e.g., Lee and Kim 1991; Komminaho et al. 1996; Papavassiliou and Hanratty 1997; Sullivan et al. 2000; Sullivan and McWilliams 2002; García-Villalba et al. 2011; Pirozzoli et al. 2014; Avsarkisov et al. 2014; Richter and Sullivan 2014; Deusebio et al. 2015; Zhou et al. 2017; Lee and Moser 2018; van Hooijdonk et al. 2018; Alcántara-Ávila et al. 2019; Glazunov et al. 2019; Mortikov et al. 2019, and references therein). Needless to say that an idealized plane Couette flow and real-world industrial and geophysical SBL flows differ in many ways. We believe, however, that results from the present analysis are relevant to real-world flows, at least as far as improved understanding of essential physical processes is concerned.

Numerous numerical-simulation, experimental, and analytical studies of idealized flows with surface (mainly spanwise) heterogeneity have been performed to date. For example, the effect of spanwise surface heterogeneity was extensively studied using a rectangular closed channel-flow configuration (see, e.g., Stroh et al. 2020; Bon and Meyers 2022; Bon et al. 2023, and references therein). Results from these three studies pertinent to the present discussion are briefly outlined below. To the best of the authors' knowledge, no comparative analysis of the plane Couette flows with spanwise and streamwise heterogeneity was performed so far.

Stroh et al. (2020) performed a DNS study of momentum and scalar transfer in a neutrally-stratified channel with streamwise triangular ridges ca. one channel depth apart. Two ridge arrangements were considered: a symmetric arrangement, and a staggered arrangement with the upper-wall ridges shifted by 1/2 of a ridge separation. In order to analyze the various flow statistics and the structure of secondary circulations generated by the surface heterogeneity patterns, a triple decomposition of the flow variables into mean, dispersive, and random parts was used. It was found (among other things) that the presence of ridges enhances momentum and passive scalar transfer by about 30% relative to a channel with homogeneous smooth walls. The global flow properties, like the skin friction coefficient and the Stanton number, are altered in a similar way in both symmetric and staggered configurations. However, the two arrangements of ridges generate different secondary circulations and change the partitioning between dispersive and random contributions to the flow statistics (with a weaker dispersive contribution in the symmetric configuration).

Bon and Meyers (2022) considered a stably-stratified channel flow with the surface spanwise heterogeneity in the form of alternating cold and warm strips. Both in-phase and antiphase arrangements were used (in the latter, the warm strips at the upper wall are at the same spanwise location as the cold strips at the lower wall). A series of direct numerical simulations was performed to cover a wide range of the Reynolds and Richardson numbers and the strip widths, and the triple decomposition of the flow fields was used for the analysis. The spanwise surface thermal heterogeneity induces secondary flows in the plane normal to the mean flow direction, similar to the secondary motions induced by heterogeneous surface roughness. The secondary motions modulate the mean streamwise velocity, generating low-momentum pathways (above the warm strips) and high-momentum pathways (above the cold strips). The streamwise velocity variations are up to 35% of the bulk streamwise velocity. In the low Reynolds number simulations, the skin friction is more than doubled as compared to the homogeneous stably-stratified channel flows. However, high Reynolds number cases reveal drag reduction where the width of the surface temperature strips exceeds the channel depth. The wall heat transfer characterized by the Nusselt number is reduced in all heterogeneous cases as compared to the respective homogeneous cases. A triple decomposition reveals the importance of dispersive contributions for momentum and heat transfer. The dispersive stress increases with the increasing width of the surface strips. Dispersive and random contributions to the heat flux are of opposite signs. As the static stability increases, the secondary motions and the dependence of the skin friction and of the wall heat transfer on the surface heterogeneity length scale become weaker. Comparative analysis of results from in-phase and antiphase configurations shows very similar flow properties for small surface temperature strip widths. As the width increases, the in-phase configuration exhibits larger dispersive contributions to fluxes and smaller random contributions than the antiphase configuration.

Bon et al. (2023) extended the analysis of Bon and Meyers (2022) by considering the effect of the streamwise extent of the temperature patches (strips) on the mean and turbulent structure of a channel flow. It was found (among other things) that the strength of the secondary circulations and the effect of the surface thermal heterogeneity on the skin friction and heat transfer weaken as the length of the surface temperature patches (in the streamwise direction) decreases. The effect is practically negligible as the patch aspect ratio approaches one. Using the local version of the Monin-Obukhov similarity theory (Nieuwstadt 1984), the flux-gradient relationships for mean velocity and mean temperature in a stably-stratified channel flow are compared with the empirical similarity functions obtained from meteorological data. In the homogeneous cases, the flux-gradient relationships follow the local Monin-Obukhov scaling fairly well. In the heterogeneous cases with the strips of finite length, the profiles of the scaled velocity and temperature gradients follow the similarity-theory predictions only well above the surface where the dispersive stress is small. In the cases with the infinitely long patches (the flow is homogeneous in the streamwise direction), the channel-flow profiles do not match the empirical similarity functions.

There is an ample body of literature on the impact of the surface heterogeneity on the structure of the atmospheric and oceanic boundary layers. A comprehensive review of prior work is beyond the scope of the present paper. However, two atmospheric boundary-layer studies are worthy of mention in relation to the problem addressed here. Sullivan et al. (2020; 2021) used LES to examine the structure of slightly convective marine atmospheric boundary layers over thermally heterogeneous water surfaces. The flow configurations with the imposed single-sided warm and cold fronts (the sea surface temperature difference of 2 K and −1.5 K over a horizontal distance between 0.1 km and 6 km typical of the upper-ocean meso-scale or submeso-scale regimes) and the geostrophic wind blowing across and along the fronts were considered. The across-front and along-front configurations are found to differ in many respects, including the strength of the ageostrophic wind, the balance of terms in the mean-wind and the mean-temperature atmospheric boundary-layer budgets, entrainment near the boundary-layer top, and the strength and the sense of rotation (for warm vs. cold fronts) of the secondary circulations generated by the surface thermal heterogeneity. One finding relevant to the present study is that the secondary circulations have stronger effect on the surface momentum fluxes in the along-front wind configuration than in its across-front wind counterpart.

A comment is in order to clarify what is referred to as "turbulence" in the context of the present study (see also MS23). Averaging DNS model output over horizontal planes to compute turbulence statistics (see sect. 3) essentially means that turbulence incorporates all fluctuations within the model domain. In other words, turbulence comprises both nearly homogeneous and nearly isotropic small-scale fluctuations as well as non-homogeneous and non-isotropic quasi-organized coherent structures (a discussion of coherent structures in our Couette flows is given in sect. 4.6). This definition is commensurate with coarse-resolution numerical models, for which a single model grid box corresponds to the entire DNS domain, and all sub-grid scale motions (that are resolved in DNS) should be described by a turbulence closure scheme. A detailed analysis of secondary circulations generated by the surface heterogeneity patterns, using a triple decomposition of the flow fields into mean, dispersive, and random parts, is not performed in the present study. Such an analysis should be a subject of future work, particularly in view of an increasing popularity of the approach in geophysical turbulence studies (e.g., Calaf et al. 2023; Boyko and Vercauteren 2023).

An outline of the paper is as follows. The flow parameters, governing equations, and boundary conditions are described in sect. 2. An outline of the DNS code and details of the simulated cases are given in sect. 3. Results are discussed in sect. 4. The discussion is centered around the juxtaposition of HETx and HETy cases. We highlight the differences between the two pairs of simulations and attempt to find physically plausible explanations for those differences. Implications of findings of the present study for turbulence closure modelling are briefly discussed in sect. 5. In sect. 6, we present conclusions from the present study and briefly outline further steps that should (in our opinion) be made to better represent (parameterize) the surface heterogeneity effects in models of strongly stable environmental and industrial flows.

2 Flow Parameters, Governing Equations, and Boundary Conditions

A three-dimensional, stably stratified, plane Couette flow is considered. The Boussinesq approximation is used, and a linear equation of state is utilized, $\rho = \rho_r\left[1 - \alpha_T\left(\theta - \theta_r\right)\right]$. Here, ρ and ρ_r are the fluid density and the constant reference density, respectively, α_T is the thermal expansion coefficient, θ and θ_r are, respectively, the potential temperature and the constant reference potential temperature. In what follows, "potential temperature" will also be referred to as simply "temperature". The physical characteristics of our numerical fluid include the kinematic molecular viscosity ν, the molecular temperature conductivity κ, and the buoyancy parameter $\beta_i = -g_i\alpha_T$, g_i being the acceleration due to gravity. The quantities α_T, g_i, ν, and κ are taken to be constant.

In our Couette-flow configuration, the fluid depth is H, the upper wall moves with a constant velocity U_u, while the lower wall is at rest. Stable buoyancy stratification is maintained by a temperature difference $\Delta\theta = \theta_u - \theta_l$ between the upper and lower walls.

The length scale H, the velocity scale U_u, the time scale H/U_u, and the temperature scale $\Delta\theta$ are used to make the variables dimensionless, and scaled temperature $\hat{\theta} = \left(\theta - \theta_l\right)/\left(\theta_u - \theta_l\right)$ is introduced. The governing Equations are (hats over dimensionless variables are omitted to simplify notation)

$$\left(\frac{\partial}{\partial t} + u_k \frac{\partial}{\partial x_k}\right) u_i = -\frac{\partial p}{\partial x_i} + \delta_{i3} Ri\theta + \frac{1}{Re}\frac{\partial^2 u_i}{\partial x_k^2}\,, \tag{1}$$

$$\frac{\partial u_i}{\partial x_i} = 0\,, \tag{2}$$

$$\left(\frac{\partial}{\partial t} + u_i \frac{\partial}{\partial x_i}\right) \theta = \frac{1}{RePr}\frac{\partial^2 \theta}{\partial x_i^2}\,. \tag{3}$$

Here, t is time, x_i are the right-hand Cartesian co-ordinates, u_i are the velocity components, and p is the deviation of pressure from the hydrostatically balanced reference pressure divided by ρ_r. The Einstein summation convention for repeated indices is used. The origin of the reference frame is at the lower boundary, the x_1 axis is in the direction of U_u, and the x_3 axis is aligned with the gravity vector and is positive upward. In the reference frame used here, $g_i = \left(0, 0, -g_3\right)$, where g_3 is the magnitude of the gravity vector. As the vertical-velocity equation is solved for the fluctuation of u_3 about its horizontal mean, θ_r is set equal to θ_l so that the dimensionless reference temperature $\left(\theta_r - \theta_l\right)/\left(\theta_u - \theta_l\right)$ drops out from the buoyancy term on the right-hand side (r.h.s.) of Eq. (1).

The governing Eqs (1)–(3) contain three dimensionless parameters. These are the bulk Reynolds number, the Prandtl number, and the bulk Richardson number:

$$Re = \frac{U_u H}{\nu}\,, \qquad Pr = \frac{\nu}{\kappa}\,, \qquad Ri = \frac{g_3 H \alpha_T \Delta\theta}{U_u^2}\,. \tag{4}$$

Periodic boundary conditions for u_i and θ are applied in both x_1 and x_2 horizontal directions. At the horizontal upper and lower boundaries, no-slip boundary conditions are used for the velocity:

$$\begin{array}{lll} u_1 = 0\,, & u_2 = u_3 = 0 & \text{at} \;\; x_3 = 0\,, \\ u_1 = 1\,, & u_2 = u_3 = 0 & \text{at} \;\; x_3 = 1\,. \end{array} \tag{5}$$

For the temperature, the following Dirichlet boundary conditions are applied:

$$\begin{array}{ll} \theta = \delta\theta \sin\left[2\pi n x_1/L_1\right] & \text{at} \;\; x_3 = 0\,, \\ \theta = 1 + \delta\theta \sin\left[2\pi n\left(x_1 - U_u t\right)/L_1\right] & \text{at} \;\; x_3 = 1\,, \end{array} \tag{6}$$

in the simulations with the streamwise heterogeneity (HETx cases, see the next section for details of the simulations performed), and

$$\begin{array}{ll} \theta = \delta\theta \sin\left[2\pi n x_2/L_2\right] & \text{at} \;\; x_3 = 0\,, \\ \theta = 1 + \delta\theta \sin\left[2\pi n x_2/L_2\right] & \text{at} \;\; x_3 = 1\,, \end{array} \tag{7}$$

in the simulations with the spanwise heterogeneity (HETy cases). Here, L_1 and L_2 are the domain sizes in the x_1 and x_2 horizontal directions, respectively, $\delta\theta$ is the (dimensionless) amplitude of the temperature variations at the upper and lower walls, and n is the number of surface temperature waves. In the homogeneous case (HOM), $\delta\theta = 0$. In all heterogeneous cases, $\delta\theta > 0$ but, importantly, the horizontal-mean surface temperature is the same in all cases. The flow domain, including the surface boundary conditions, is sketched in Fig. 1. Note that for illustration purposes arbitrary (dimensionless) domain sizes are used

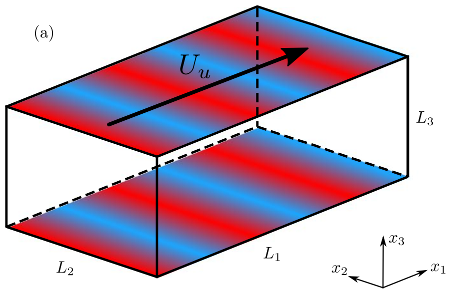

Fig. 1 A sketch of the Couette flow configuration with the streamwise (**a**) and spanwise (**b**) surface thermal heterogeneity

in Fig. 1, whereas $L_1 = L_2 = 8$ and the vertical domain size $L_3 = 1$ is used in all simulations (see sect. 3).

Note that the boundary conditions (5)–(7) ensure the flow symmetry of the Couette flow configuration. In HETx cases, the temperature waves propagate along the upper boundary in the streamwise direction with the speed U_u, generating a thermally heterogeneous upper surface matching its lower-surface counterpart. In the HETy cases, the surface-temperature minima and maxima are at the same spanwise locations at the lower and upper walls (cf. Bon and Meyers 2022; Stroh et al. 2020). Although the Couette flow configuration is highly idealized as compared to the majority of real-world flows, it has desirable features for the present analysis. There is no mean pressure gradient forcing, the average wall temperatures are constant in time, and the average total momentum and temperature fluxes are height-constant. As a result, stationary statistics are acquired by long temporal integration even under strongly stable intermittent flow conditions.

3 Simulated Cases

The DNS code used in the present study utilizes pseudospectral differencing in the horizontal directions (using fast Fourier transforms) and second-order finite differencing in the vertical direction. The upper 1/3 wavenumbers are truncated at each time step for dealiasing. A staggered configuration is used in the vertical direction with the horizontal velocity components, temperature, and pressure placed half-way between the vertical velocity component. The divergence free condition is enforced by solving a Poisson equation for the fluctuating pressure. A third-order three-substep Runge-Kutta scheme is used for time advancement, and the time step is adjusted dynamically based on a fixed Courant-Fredrichs-Lewy condition. The code parallelization is based on a two-dimensional domain decomposition using the Message Passing Interface. The algorithm makes it possible to effectively run the code on massively parallel computer systems using a large number of processors (in excess of 10^4). The DNS code and the code parallelization are described in much detail in Sullivan et al. (2000), Sullivan and McWilliams (2002), and Sullivan and Patton (2011). Readers are referred to the above papers for a comprehensive account.

One simulation with homogeneous lower and upper walls (HOM) and four simulations with heterogeneous walls (HET) are analyzed. The domain size in both horizontal directions is 8, the domain size in the vertical direction is 1, and the number of grid points is 512, 512, and 256 in the streamwise x_1, spanwise x_2, and vertical x_3 directions, respectively.

The numerical mesh is uniform in the vertical direction and in both horizontal directions. In all simulations, the values of $Pr = 1$, $Re = 10^4$, and $Ri = 0.25$ are used, and the number of surface temperature waves in the heterogeneous simulations is 4. Table 1 presents governing parameters of the simulated cases.

All variables in Table 1 are made dimensionless with the scales H, U_u, H/U_u, and $\Delta\theta$. T_t is the total length of the simulation (in dimensionless time units H/U_u), T_s is the length of the sampling period at the end of the run, $Re_\tau = u_* Re$ and $Ri_\tau = u_*^{-2} Ri = Re_\tau^{-2} Re^2 Ri$ are, respectively, the Reynolds number and the Richardson number based on the surface friction velocity u_* (e.g., Gandía-Barberá et al. 2021), Q_* is the surface temperature flux, and $L = -u_*^3/\kappa Ri Q_*$ is the Obukhov length (Obukhov 1954), $\kappa = 0.4$ being the von Kármán constant. The quantity L^{-1} is a measure of static stability based on the surface fluxes. Note that the simulations HET025x and HET050x differ from the simulations HET025y and HET050y, respectively, only by the orientation of the surface heterogeneity patterns. In HETx cases, the temperature-wave crests are normal to the the mean flow, whereas in HETy cases the crests are parallel to the mean flow. The former cases (along with HOM) were used by MS23 in their analysis of the SBL structure.

The simulation HOM is initialized with a neutral, fully developed, stationary Couette flow. The stable buoyancy stratification is established by increasing Ri linearly in time over 100 dimensionless time units from $Ri = 0$ to $Ri = 0.25$. The simulation is then continued until a laminar Couette flow regime is achieved. The value of $Ri = 0.25$ appears to be sufficiently large to fully extinguish turbulence in the homogeneous case. As the stability measures Ri_τ and L^{-1} suggest (Table 1), all our simulations are in the very stable regime (except perhaps HET050y). DNSs of open channel flow performed by Nieuwstadt (2005) indicate that turbulence is not sustained when $L^{-1} > 0.5$ (the definition of L used in op. cit. is modified to match the present definition).

The heterogeneous simulations HETx and HETy start with $Ri = 0$, $\delta\theta = 0$, and a linear velocity profile. Velocity and temperature fluctuations taken from the neutral turbulent Couette flow are added in the lower 1/4 and the upper 1/4 of the flow domain to aid turbulence spin-up. The Richardson number is increased from $Ri = 0$ to $Ri = 0.25$ over 10 time units, while the temperature difference $\delta\theta$ is increased from zero to its value given in Table 1 over 100 time units. The heterogeneous simulations are carried forward until a quasi-stationary flow regime is established. The flow is viewed as stationarity when the average fluxes of momentum and scalar are height-constant.

The DNS model output is averaged over horizontal planes, and the resulting vertical profiles are then averaged over several thousand time steps. The number of time samples differs between the cases (see Table 1), but the sampling period in the HETx and HETy cases covers more than 160 time units. These horizontal and time mean quantities are treated as approximations to the ensemble-mean quantities. In the following, an overbar denotes a horizontal-mean quantity, a prime denotes a fluctuation about a horizontal

Table 1 Governing parameters of simulations

Case	$\delta\theta$	T_t	T_s	Re_τ	$Ri_\tau \times 10^3$	$Q_* \times 10^5$	L^{-1}
HOM	0.00	1115	15	104.63	2.284	−10.93	9.54
HET025x	0.25	1166	166	100.50	2.475	−9.80	9.65
HET050x	0.50	1392	392	107.77	2.153	−7.45	5.95
HET025y	0.25	1908	908	114.85	1.895	−9.49	6.26
HET050y	0.50	864	466	207.95	0.578	−20.45	2.27

mean, and the angle brackets denote quantities averaged over time [the sole exceptions are Eqs. (15) and (16) in sect. 5 where the angle brackets denote the Reynolds averaging].

Apart from the results from the homogeneous simulation HOM and four heterogeneous simulations HET025x, HET050x, HET025y, and HET050y (whose comparative analysis is the major focus of the present study), results from a neutral turbulent Couette-flow simulation are shown in Fig. 5. The neutral run is similar to HOM but $Ri = 0$ and $T_s = 100$.

4 Results

4.1 Mean Fields

Figure 2 shows vertical profiles of the streamwise component of mean velocity, $U = \left\langle \overline{u}_1 \right\rangle$, and mean temperature, $\Theta = \left\langle \overline{\theta} \right\rangle$. In the homogeneous case, the profiles of both U and Θ are linear. These profiles correspond to the laminar Couette-flow regime. Although we give turbulence a good chance to survive by starting the homogeneous simulation with a fully turbulent neutral flow and gradually increasing the Richardson number, the buoyancy stratification at $Ri = 0.25$ is strong enough to fully quench turbulence.

As seen from Fig. 2, the mean velocity profile is little affected by the surface thermal heterogeneity in both HETx cases. The mean flow gradient is only slightly different from the laminar Couette value. In HETy cases, the effect of heterogeneity is more pronounced, particularly in the simulation HET050y, where the mean streamwise velocity deviates considerably from the linear profile. It is interesting to note that the mean gradient $\partial U/\partial x_3 > 1$ in the middle of the domain in both HETx cases and in HET025y. In HET050y, $\partial U/\partial x_3 < 1$ in most of the domain (apart from the near-wall regions, where the mean velocity gradient is increased due to no-slip boundary conditions), indicating enhanced mixing of mean velocity in the flows with spanwise heterogeneity. The mean temperature profile is more sensitive to the surface thermal heterogeneity than the mean velocity profile. As $\delta\theta$ increases, the flow becomes increasingly mixed with respect to Θ

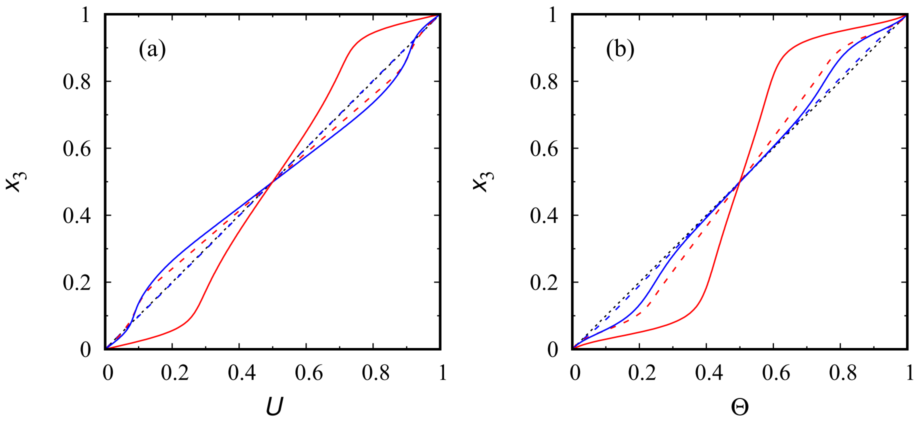

Fig. 2 Streamwise component of mean velocity (**a**) and mean temperature (**b**) from simulations HET025x (blue dashed curves), HET050x (red dashed curves), HET025y (blue solid curves), and HET50y (red solid curves). Black dotted lines show the laminar solution

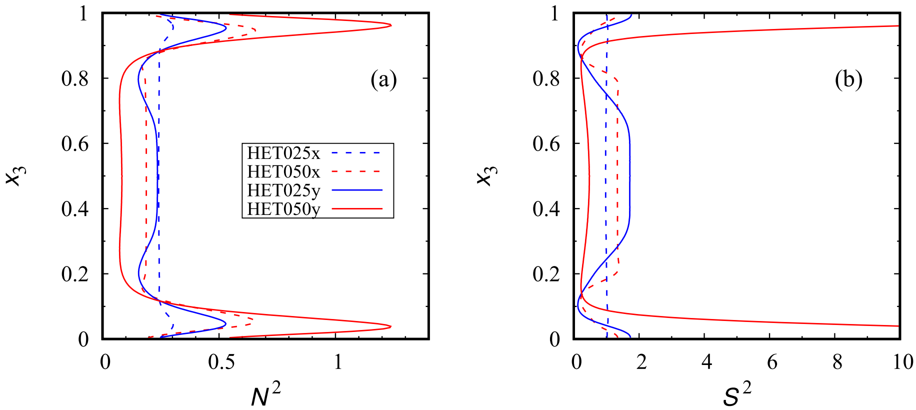

Fig. 3 The squared buoyancy frequency N^2 (**a**) and the squared shear frequency S^2 (**b**) from simulations HET025x (blue dashed), HET050x (red dashed), HET025y (blue solid), and HET50y (red solid)

Fig. 4 The gradient Richardson number Ri_g from heterogeneous cases

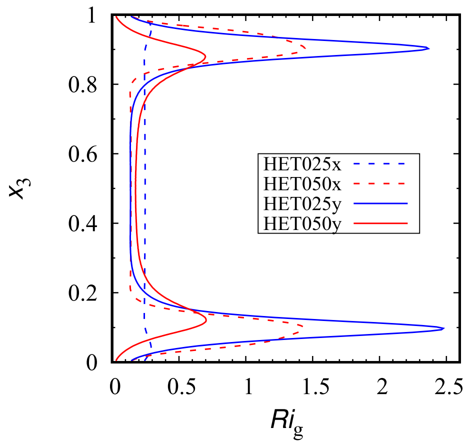

away from the walls. The effect of surface thermal heterogeneity on both mean velocity and mean temperature is stronger in the HETy simulations than in the HETx simulations. Note that in simulation HET025x, where $\delta\theta$ is comparatively small, the effect of streamwise surface heterogeneity is weak, and both the velocity and the temperature profiles are nearly linear. This is at variance with simulation HET025y, where even relatively small $\delta\theta$ appears to be sufficient to appreciably influence the U and Θ profiles.

Vertical profiles of the dimensionless squared shear and buoyancy frequencies, S^2 and N^2, respectively, and of the gradient Richardson number, Ri_g, are shown in Figs. 3 and 4. Here,

$$S^2 = \left(\frac{\partial U}{\partial x_3}\right)^2 , \qquad N^2 = Ri\frac{\partial \Theta}{\partial x_3} , \qquad Ri_g = \frac{N^2}{S^2} . \tag{8}$$

Examination of Figs. 3 and 4 reveals a complex dependence of the above quantities on $\delta\theta$, which is quite different in HETx and HETy cases. As discussed above, both the U and Θ profiles are only slightly different from the linear profiles in a weakly turbulent HET025x case. As a result, the gradient Richardson number is nearly height-constant equal to 0.25. In HET050x, Ri_g peaks near the boundaries (at about $x_3 = 0.1$ and $x_3 = 0.9$), whereas in the middle of the domain Ri_g is reduced as compared to $Ri_g \approx 0.25$ in HET025x. This behaviour of Ri_g in HET050x reflects an enhanced mixing with respect to Θ away from the walls and a larger sensitivity of Θ to the surface thermal heterogeneity as compared to U (see above). The situation is different in the HETy cases with the spanwise heterogeneity. As seen from Fig. 3, an increase in $\delta\theta$ leads to reduced values of both S^2 and N^2 in the middle of the flow domain and to larger peaks of both S^2 and N^2 near the walls. The gradient Richardson number (Fig. 4) in the middle of the flow is larger in HET050y than in HET025y, but the Ri_g maxima near the walls in HET050y are reduced. This is at variance with the HETx cases, where larger values of $\delta\theta$ result in a reduced Ri_g in the the middle of the flow and larger Ri_g maxima near the walls.

Figures 5 and 6 show profiles of the streamwise mean-velocity component and of temperature in wall units $\left(U^+, \Theta^+, x_3^+\right) = \left(U/u_*, -\Theta u_*/Q_*, x_3 Re_\tau\right)$. The flow is well resolved in our simulations. The first grid point above the surface is $x_3^+ \approx 0.2$, except for the case HET050y where it is $x_3^+ \approx 0.4$. Although a larger grid spacing may be used in neutral Couette flows, the resolution cannot be compromised in our simulations. The large temperature gradients in the near-wall thermal boundary layers should be resolved; it is these temperature (buoyancy) gradients that drive turbulence in the heterogeneous simulations. As mentioned in MS23, results from test runs with lower resolution in the vertical direction are quantitatively and even qualitatively different from the results of high-resolution simulations and are not faithful. The domain size in the horizontal directions cannot be compromised either because of the need to simulate large-scale elongated structures characteristic of plane Couette flows (e.g., Komminaho et al. 1996; Papavassiliou and Hanratty 1997; Pirozzoli et al. 2014; Avsarkisov et al. 2014; Jiménez 2018; Lee and Moser 2018).

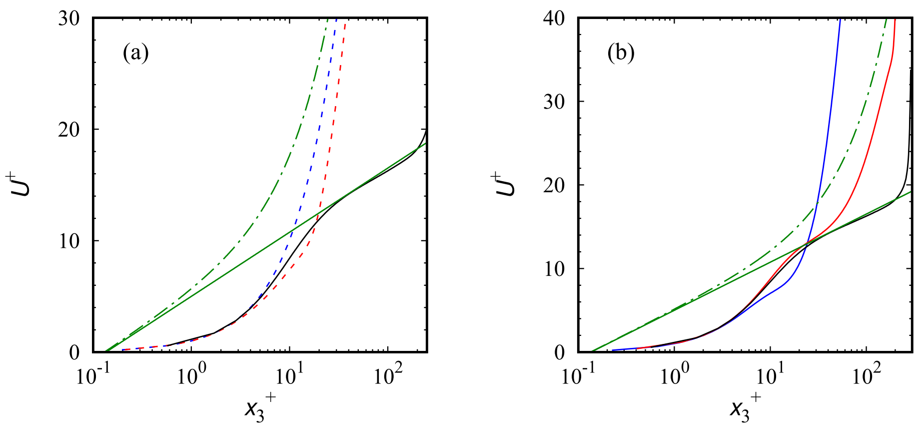

Fig. 5 Streamwise mean-velocity profiles in wall units. Dashed curves in (**a**) show the profiles from simulations HET025x (blue) and HET050x (red), and solid curves in (**b**) – from simulations HET025y (blue) and HET050y (red). Black and green solid lines show the profiles from the neutrally stratified Couette flow and the logarithmic velocity profile, respectively. Green dot-dashed lines show the Monin-Obukhov log-linear velocity profile computed with the surface friction velocity and the surface buoyancy flux from simulations HET050x (**a**) and HET050y (**b**)

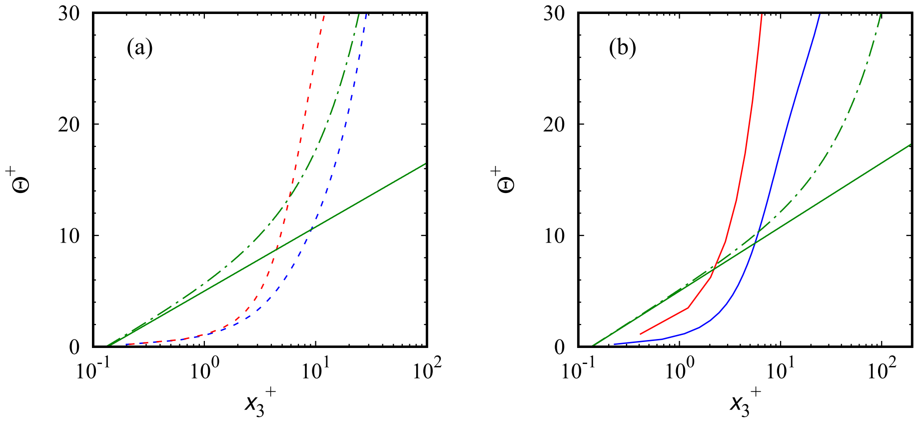

Fig. 6 Temperature profiles in wall units. Dashed curves in (**a**) show the profiles from simulations HET025x (blue) and HET050x (red), and solid curves in (**b**) – from simulations HET025y (blue) and HET050y (red). Green solid lines show the logarithmic temperature profile. Green dot-dashed lines show the Monin-Obukhov log-linear temperature profile computed with the surface friction velocity and the surface buoyancy flux from simulations HET050x (**a**) and HET050y (**b**)

Black and green solid lines in Fig. 5 show, respectively, the streamwise velocity from the neutral Couette-flow simulation and the logarithmic velocity profile

$$U^+ = \frac{1}{\kappa} \ln\left(x_3^+\right) + B_0 \,, \tag{9}$$

where $B_0 = 5.0$ is a dimensionless constant. The velocity profile from neutral simulation closely follows the log-profile over the height range $20 \le x_3^+ \le 200$. This is not the case for the heterogeneous cases, neither in HETx nor in HETy simulations, where the velocity profiles do not follow the log-layer scaling.

The green dot-dashed curves in Figs. 5 and 6 show the log-linear velocity and temperature profiles (Obukhov 1954; Monin and Obukhov 1954; Monin and Yaglom 1971)

$$\left(U^+, \Theta^+\right) = \frac{1}{\kappa} \ln\left(x_3^+\right) + B_0 + \frac{C_u}{\kappa} \frac{x_3^+}{L^+} \,, \tag{10}$$

where $C_u = 5$ is a dimensionless constant, and $L^+ = LRe_\tau$ is the Obukhov length in wall units. The profiles are computed using u_* and Q_* from simulations HET050x and HET050y and external parameters Re and Ri. As seen from Figs. 5 and 6, neither the velocity profiles nor the temperature profiles follow the log-linear scaling given by Eq. (10) (cf. the results of Bon et al. 2023). This is actually not surprising. Recall that the Monin-Obukhov surface-layer flux-profile relationships are developed for turbulent layers over homogeneous surfaces. Strictly speaking, they cannot be applied if the assumption of surface homogeneity is not fulfilled (although it is often done in practice, e.g., in atmospheric modelling). Different flux-profile relationships are required for thermally heterogeneous surfaces.

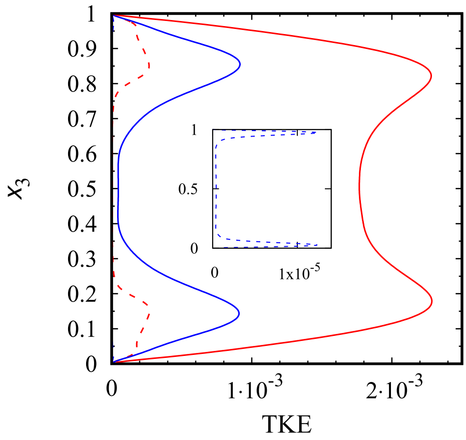

Fig. 7 Turbulence kinetic energy. The line types are the same as in Figs. 3 and 4

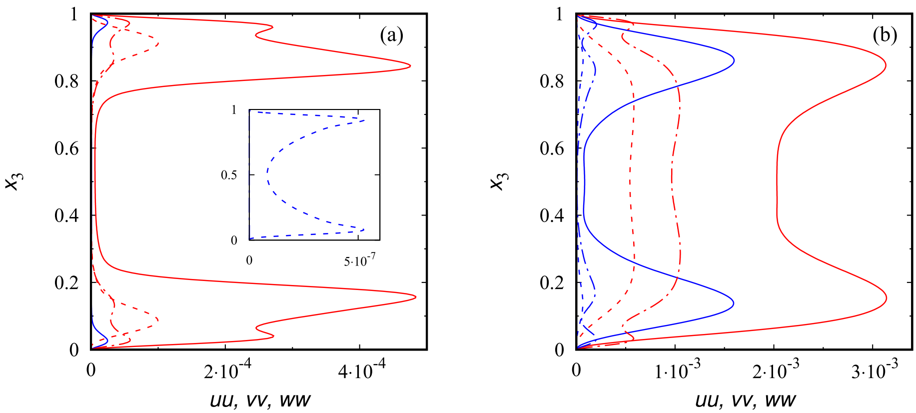

Fig. 8 Streamwise (solid curves), spanwise (dot-dashed curves), and vertical (dashed curves) velocity variance from simulations (**a**) HET025x (blue) and HET050x (red), and (**b**) HET025y (blue) and HET50y (red)

4.2 Variances

Figure 7 shows vertical profiles of turbulence kinetic energy TKE= $\frac{1}{2}\left\langle \overline{u_i'^2} \right\rangle$. As could be expected, TKE increases with increasing amplitude of the surface temperature variations. The level of turbulence is very low in the case HET025x. The value of $\delta\theta = 0.25$ is too small to make the flow noticeably turbulent in the regime, where the temperature-wave crests are normal to the mean flow (see the dashed blue line in the insert, that line is hardly seen on the scale of the main plot in Fig. 7). However, the flow is noticeably turbulent in the HET025y case, where the temperature-wave crests are parallel to the mean flow. Generally, TKE is much larger in the HETy cases than in the HETx cases, indicating that the orientation of the surface heterogeneity patterns is of decisive importance for setting the turbulence intensity.

Velocity variances $uu = \left\langle \overline{u_1'^2} \right\rangle$ (streamwise), $vv = \left\langle \overline{u_2'^2} \right\rangle$ (spanwise), and $ww = \left\langle \overline{u_3'^2} \right\rangle$ (vertical) are shown in Fig. 8. In all simulations, the largest contribution to the TKE is uu.

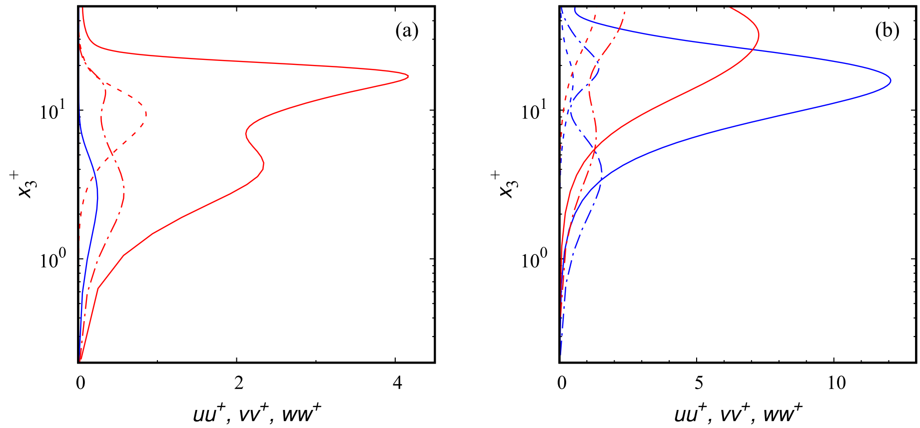

Fig. 9 The same as in Fig. 8 but in wall units for the lower part of the model domain

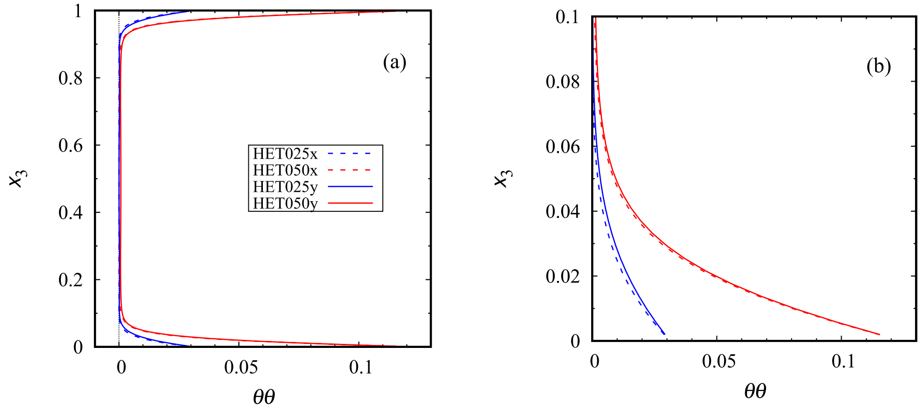

Fig. 10 (**a**) Temperature variance from heterogeneous cases. (**b**) The same as in (**a**) but for the lower part of the domain

It is dominant in a weakly turbulent case HET025x (see MS23), but all three velocity variances are very small in HET025x [vv is entirely negligible, it is not seen even on the scale of the insert in Fig. 8a]. In simulations HET050x and HET025y, vv and ww are substantial, although still several times smaller than uu. In the HET050y case, both vv and ww become commensurate with uu.

Figure 9 shows the velocity variances in wall units (i.e., $uu^+ = uu/u_*^2$, $vv^+ = vv/u_*^2$, and $ww^+ = ww/u_*^2$ as function of $x_3^+ = x_3 Re_\tau$). This figure provides details of the near-wall behaviour of the velocity variances. Note that the shape of the velocity-variance profiles is very different in the HETx and HETy cases. There is no clear tendency for the velocity variances to collapse on the same curve (neither for uu^+, nor for vv^+ or ww^+) when the surface friction velocity is used for normalization.

As would be expected, the temperature variance $\theta\theta = \left\langle \overline{\theta'^2} \right\rangle$ increases with the increasing $\delta\theta$, see Fig. 10. The large values of $\theta\theta$ are limited to the near vicinity of the lower and upper walls. In the bulk of the flow interior $0.1 \leq x_3 \leq 0.9$, the temperature variance is small. It is significant that the orientation of the surface heterogeneity patterns has practically no effect on the temperature variance. As seen from Fig. 10, the values of $\theta\theta$ in simulations HET025x and HET025y basically coincide, and the same holds for HET050x and HET050y.

4.3 Turbulence Anisotropy

One measure of the turbulence anisotropy is the departure-from-isotropy tensor (see, e.g., Pope 2000)

$$b_{ij} = \frac{\left\langle \overline{u_i' u_j'} \right\rangle}{\left\langle \overline{u_k'^2} \right\rangle} - \frac{1}{3}\delta_{ij} \,. \tag{11}$$

In isotropic turbulence, all components of b_{ij} are zero. If velocity fluctuations in one direction are suppressed, turbulence tends towards the two-component limit, and the respective diagonal component of b_{ij} is equal to $-1/3$. Figure 11 shows that $b_{33} < 0$ in simulations HET050, HET025y, and HET050y. This indicates a tendency towards a two-component state, where the vertical-velocity fluctuations (aligned with the vector of gravity) are suppressed by buoyancy and the TKE is dominated by the horizontal velocity fluctuations. In simulation HET025x, b_{33} is slightly positive in small regions near the upper and lower boundaries. However, turbulence in HET025x is very weak and all three velocity variances are negligibly small, see Figs. 7 and 8.

There is a notable difference between the shape of the b_{33} profiles in HETx and HETy simulations. In HET050x, for example (red dashed curve in Fig. 11), there are pronounced b_{33} maxima near the lower and upper boundaries of the domain, at $x_3 \approx 0.1$ and $x_3 \approx 0.9$, respectively. Results from simulation HET075x with $\delta\theta = 0.75$ (not shown here, see Fig. 7 in MS23) reveal a similar behaviour of b_{33}. In HET050y (red solid curve in Fig. 11), no maxima near the upper and lower boundaries of the domain are seen. The b_{33} component of the departure-from-isotropy tensor monotonically increases from the walls, where the vertical-velocity fluctuations are strongly suppressed (by the wall) and turbulence is nearly

Fig. 11 The b_{33} component of the departure-from-isotropy tensor, Eq. (11). The line types are the same as in Figs. 3, 4, and 10

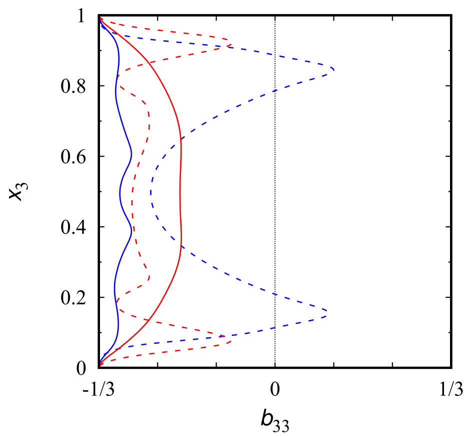

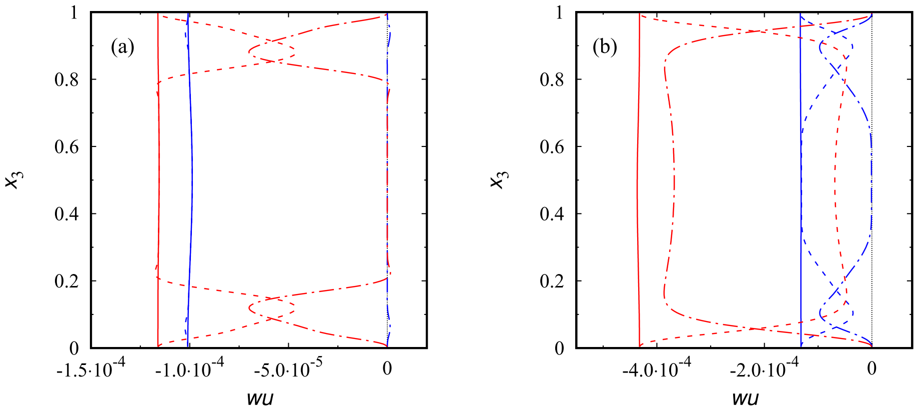

Fig. 12 Vertical flux of streamwise momentum from simulations (**a**) HET025x (blue) and HET050x (red), and (**b**) HET025y (blue) and HET50y (red). Solid curves show total (turbulent plus molecular) flux, and dot-dashed and dashed curves show contributions due to turbulence and due to molecular diffusion, respectively

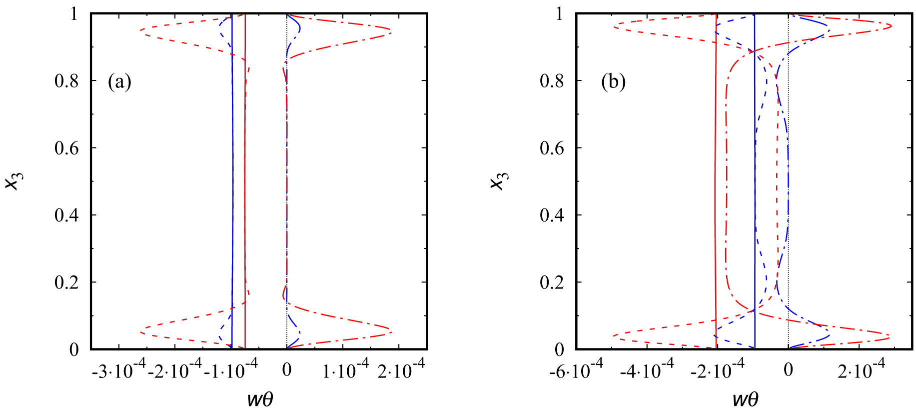

Fig. 13 Vertical component of the temperature flux from simulations (**a**) HET025x (blue) and HET050x (red), and (**b**) HET025y (blue) and HET50y (red). The line types are the same as in Fig. 12

two-component, towards the central part of the flow domain, where the vertical-velocity fluctuations are substantial and turbulence tends to the isotropic state.

4.4 Fluxes

Figures 12 and 13 show vertical profiles of the vertical flux of streamwise momentum (denoted wu) and vertical temperature flux (denoted $w\theta$), respectively. The total fluxes, i.e., the sum of molecular and turbulent fluxes, are depth-constant in the steady state. That is

$$\left\langle \overline{u_3' u_1'} \right\rangle - \frac{1}{Re} \frac{\partial \left\langle \overline{u_1} \right\rangle}{\partial x_3} = const\,, \tag{12}$$

and

$$\left\langle \overline{u_3'\theta'} \right\rangle - \frac{1}{PrRe}\frac{\partial \left\langle \overline{\theta} \right\rangle}{\partial x_3} = const\,. \tag{13}$$

In the laminar Couette flow, wu and $w\theta$ are due to molecular diffusion only, and the total fluxes are equal to Re^{-1} and $(PrRe)^{-1}$, respectively.

As shown in Fig. 12, the turbulent momentum flux is very small in the simulation HET025x, and the total flux is practically the same as in the laminar flow. This is different in the simulation HET025y, where the turbulent flux is substantial. Generally, the magnitude of wu increases with the increasing amplitude of the surface temperature variations. The increase is more significant in the HETy cases (e.g., wu in HET050y is about four times larger than in HET050x). In all simulations, both the turbulent and molecular fluxes contribute to downward momentum transport. That is, both molecular diffusion and turbulence transfer momentum down the gradient of the mean streamwise velocity.

The behaviour of the vertical temperature flux, Fig. 13, is more complex. In a weakly turbulent case HET025x, the total flux is close to the laminar value. However (as different from the streamwise momentum flux), the turbulent contribution $\left\langle \overline{u_3'\theta'} \right\rangle$ is not entirely negligible. In cases HET025x, HET050x, and HET025y, the magnitude of the total vertical temperature flux is reduced (relative to the laminar value) as $\delta\theta$ is increased. This is different in HET050y, where the magnitude of $w\theta$ is about twice as large as in the laminar flow. An outstanding feature of the heterogeneous simulations is the sign of the turbulent contribution to $w\theta$ near the upper and lower boundaries. The turbulent flux proves to be positive, although the flow is stably stratified in the mean and the total (molecular plus turbulent) vertical temperature flux is negative. Eddy motions generated by the surface thermal heterogeneity cause heat transfer up the gradient of the mean temperature. This is analogous to convective boundary-layer flows, where counter-gradient heat transport is often encountered and is attributed to quasi-organized cell-like structures whose spatial scale is large as compared to the scale of chaotic, nearly isotropic turbulent motions. It is important to note (see Fig. 13) that the turbulent vertical temperature flux in the middle of the domain is nearly zero in the cases HET025x, HET050x, and HET025y. This is different in the case HET050y (Fig. 13b), where turbulent flux in the middle of the domain is large and negative (down the gradient of mean temperature). It is this negative $\left\langle \overline{u_3'\theta'} \right\rangle$ that is largely responsible for the increased magnitude of the total vertical temperature flux in HET050y. In the other three heterogeneous simulations, the turbulent flux $\left\langle \overline{u_3'\theta'} \right\rangle$ is mostly positive, leading to a reduced magnitude of $w\theta$.

The streamwise component of the temperature flux (denoted $u\theta$) is shown in Fig. 14. Note that due to periodic boundary conditions in the x_1 and x_2 directions horizontally averaged molecular flux is zero, and the contributions to $u\theta$ are solely due to turbulence. There is a striking difference between the HETx and HETy cases. In HETx cases, $u\theta$ is nearly zero in the middle of the flow domain and has pronounced maxima close to the upper and lower walls. In HETy cases, $u\theta$ is zero to positive in the middle of the domain and has pronounced minima close to the walls. Visualization of the flow structure in sect. 4.6 helps explain the behaviour of $u\theta$.

Fig. 14 Streamwise component of the temperature flux. The line types are the same as in Figs. 3, 4, and 10

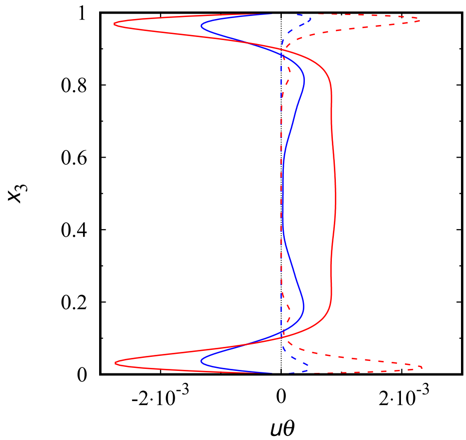

4.5 Skewness

Vertical profiles of the vertical-velocity and temperature skewness,

$$S_w = \frac{\langle \overline{u_3'^3} \rangle}{\langle \overline{u_3'^2} \rangle^{3/2}} \quad \text{and} \quad S_\theta = \frac{\langle \overline{\theta'^3} \rangle}{\langle \overline{\theta'^2} \rangle^{3/2}}, \tag{14}$$

are shown in Fig. 15. In all four HET cases, $S_w > 0$ and $S_\theta > 0$ near the lower wall, and (by symmetry about the mid-plane $x_3 = 1/2$) $S_w < 0$ and $S_\theta < 0$ near the upper wall. The values of S_w and S_θ are indicative of localization (fractional area coverage) of positive/negative vertical-velocity and temperature fluctuations about their horizontal-mean values. Positive S_w and S_θ in the lower part of the domain indicate that positive (upward) vertical velocity and positive temperature fluctuations cover a smaller fractional area as compared to their negative counterparts. Similar arguments hold for the upper part of the domain, where

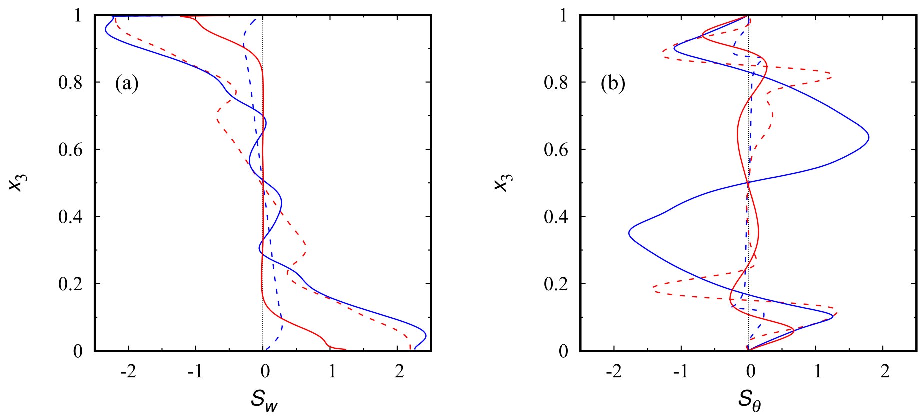

Fig. 15 (**a**) Vertical-velocity skewness and (**b**) temperature skewness. The line types are the same as in Figs. 3, 4, and 10

$S_w < 0$ and $S_\theta < 0$ indicate stronger localization of negative (downward) vertical velocity and negative temperature fluctuations.

As far as the skewness is concerned, there is a close analogy between our stably-stratified Couette flow with thermally heterogeneous surfaces and an atmospheric convective boundary layer (CBL) driven by the surface buoyancy flux (e.g., Lenschow et al. 2012). In the atmospheric CBL that grows into a stably-stratified air aloft, both S_w and S_θ are positive in the bulk of the boundary layer, where positive vertical-velocity anomalies and positive temperature anomalies are highly localized. Those anomalies are collocated, forming coherent structures (convective plumes and rolls) that account for much of the upward temperature flux and cause counter-gradient turbulent heat transfer.

Note that in the simulation HET050y S_w is nearly zero in the middle of the domain, indicating the absence of quasi-organized structures associated with the localized positive/negative vertical-velocity anomalies. This helps to understand the behaviour of the vertical turbulent temperature flux in HET050y (Fig. 13b). The turbulent flux is down-gradient (negative) in the middle of the domain, where S_w is nearly zero. The up-gradient turbulent heat transfer occurs only near the upper and lower walls, where both S_w and S_θ are substantial and of the same sign.

4.6 Visualization of Flow Structure

Figure 16 (which is adopted from MS23, see Fig. 13 in op. cit.) shows fluctuations of vertical velocity, u_3', and of potential temperature, θ', in an $x_1 - x_2$ plane just above the lower wall for simulation HET050x with the streamwise surface heterogeneity. This and all other

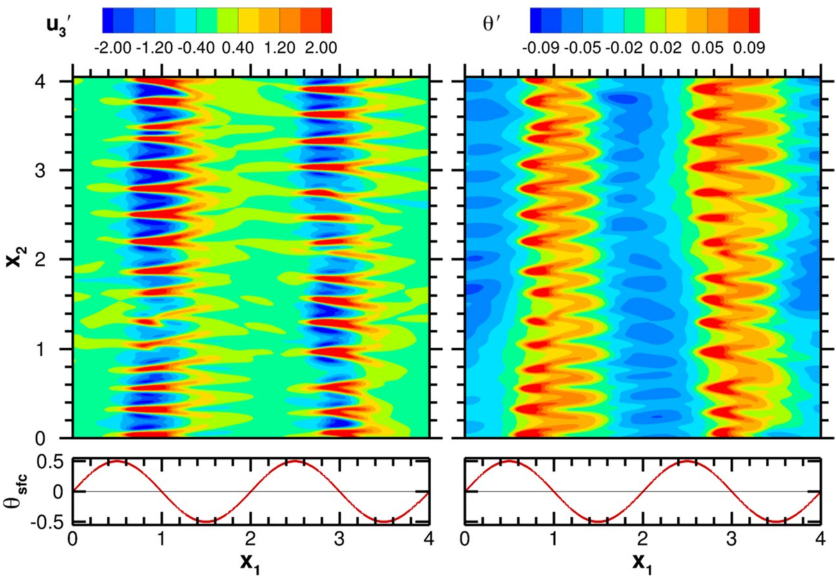

Fig. 16 Horizontal cross sections of the fluctuations of vertical velocity (left panel) and potential temperature (right panel) about their horizontal mean values for simulation HET050x. To highlight details only 1/4 of numerical domain is shown. Red (blue) colours correspond to positive (negative) values of u_3' ($\times 10^2$) and θ' as shown in the colour scale bars. For reference the spatial variation of the imposed surface temperature θ_{sfc} is shown in the bottom panel of each figure

cross sections are taken near the end of the sampling period at $x_3 = 0.076$ ($x_3^+ = 8.19$ for HET050x, and $x_3^+ = 15.80$ for HET050y). The most vigorous positive and negative vertical velocity fluctuations are concentrated at the same streamwise locations $x_1 \approx (0.9, 2.9)$. There are quiescent nearly laminar regions at intermediate locations $x_1 \approx (2, 4)$. The vigorous fluctuations in u_3' occur roughly 70 degrees forward of the peak surface temperature but behind the location of maximum $-\partial\theta_{sfc}/\partial x_1$ at $x_1 = (1, 3)$. Horizontal advection in the near-wall region transports high amplitude fluctuations forward of the location of the peak surface temperature variation, similar to weakly stratified heterogeneous flows (see, e.g., Stoll and Porté-Agel 2009, and MS16). Apparently the temperature field responds more rapidly to the surface boundary conditions than streamwise velocity. It should be stressed that the spatially intermittent flow structures in our very stable HETx simulations are noticeably different from the tilted temperature fronts encountered in weakly stable, continuously turbulent boundary-layer flows over homogeneous surfaces (e.g., García-Villalba et al. 2011; Chung and Matheou 2012; Sullivan et al. 2016; Glazunov et al. 2019).

Figure 17 shows vertical-velocity and temperature fluctuations for simulation HET050y with the spanwise surface heterogeneity. Elongated structures of large positive u_3' and θ' are readily identified, separated by more quiescent regions with relatively small temperature fluctuations. These structures are locked to the (spanwise) positions of the surface temperature maxima and span the entire flow domain in the streamwise direction. This is at variance with HET050x, where regions of large positive u_3' and θ' have smaller spatial scales and are rather intermittent in both spanwise and streamwise directions.

Coherent patterns of strong positive u_3' are nearly collocated with the patterns of strong positive θ' in both HET050x and HET050y simulations (Figs. 16 and 17). The fluctuation u_3' and θ' are spatially correlated, leading to positive (upward) turbulent temperature flux over a sizable part of the flow domain, Fig. 18 (apart from minor details, the left panel of Fig. 18 is the same as Fig. 14a in MS23). Note that the local values of $u_3'\theta'$ are an order of magnitude larger than the horizontally averaged flux $\overline{u_3'\theta'}$. Positive values of $u_3'\theta'$ are more localized (have a smaller fractional area coverage) than negative

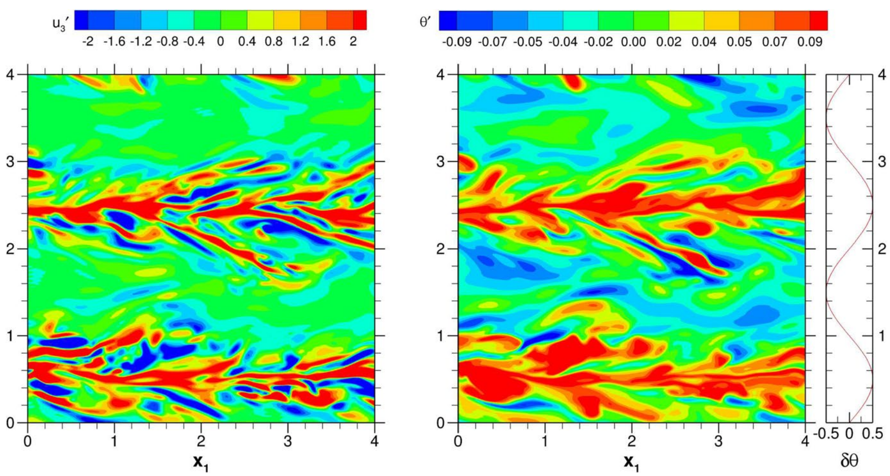

Fig. 17 The same as in Fig. 16 but for simulation HET050y. The spatial variation of the imposed surface temperature θ_{sfc} is shown to the right of the θ' figure

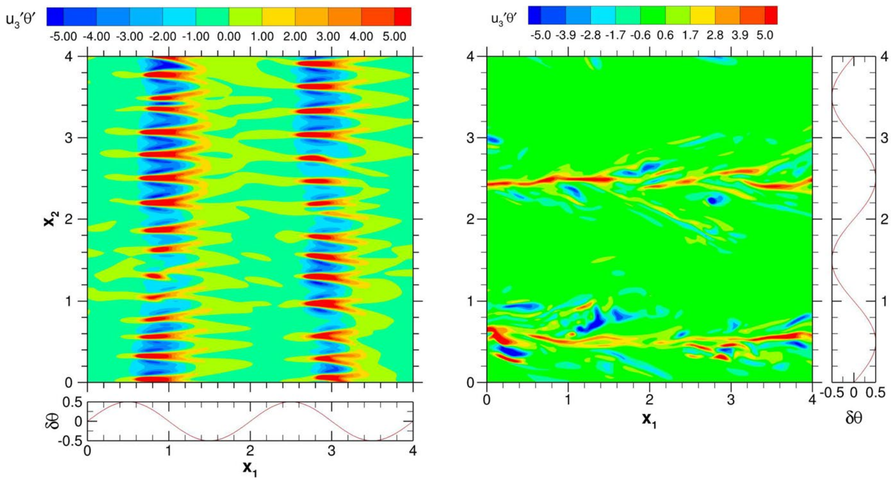

Fig. 18 Horizontal cross section of the vertical temperature flux for simulations HET050x (left) and HET050y (right). Red (blue) colours correspond to positive (negative) values of the temperature flux ($\times 10^3$) as shown in the colour scale bars. The spatial variation of the imposed surface temperature θ_{sfc} is shown for each figure

to nearly-zero values of $u_3'\theta'$, particularly in HET050y. However, their amplitude is large. As a result, the horizontal-mean vertical turbulent temperature flux appears to be positive. Importantly, the flow remains stably stratified in a horizontal mean sense, and the total (molecular plus turbulent) flux remains negative, i.e., down the gradient of mean temperature. Visualization of the flow eddy structure lends support to the explanation of positive vertical turbulent temperature flux suggested by the vertical-velocity and temperature skewness.

Although the overall behaviour of the vertical temperature flux is similar in HET050x and HET050y cases (collocation of strong positive u_3' and θ' fluctuations leads to counter-gradient turbulent heat flux), there is a notable difference between the flows with the streamwise and spanwise surface heterogeneity. Examination of Fig. 18 reveals that coherent patterns in HET050x and HET050y differ considerably in terms of size and location. In HET050y, narrow streaks of large positive $u_3'\theta'$ locked to the surface temperature maxima span the entire flow domain in the streamwise directions. There are several relatively small spots of large negative $u_3'\theta'$ but positive $u_3'\theta'$ patterns dominate. The streaks are separated by wide areas of nearly zero $u_3'\theta'$. In HET050x, the spatial scales, shapes, and location of coherent structures are very different. The size of the "arrowhead-shaped" regions of relatively large positive $u_3'\theta'$ is ca. $0.6 - 0.8$ in streamwise direction and ca. $0.2 - 0.3$ in the spanwise direction. The regions of large positive $u_3'\theta'$ are located slightly downstream of the surface temperature maxima, with the regions of negative $u_3'\theta'$ between the arrowhead-shaped patterns. Large areas between the coherent $u_3'\theta'$ patterns (green areas in Fig. 18, left panel) are characterized by nearly zero vertical temperature flux.

The above consideration of Figs. 16 – 18 suggests a qualitative explanation of enhanced vertical mixing in the flows with the spanwise surface heterogeneity as compared to their spanwise heterogeneous counterparts. Consider the situation near the lower wall. In both HETx and HETy configurations, surface thermal heterogeneity generates local convective instabilities over warm regions (where buoyancy exceeds the horizontal-mean buoyancy). Convectively generated turbulence is then advected in the streamwise direction. In HETy cases, advection takes place over the lines of surface temperature maxima, which further support convective motions. In HETx case, convectively generated turbulence is advected over cold regions, where the strength of buoyancy stratification is locally increased. As a result, more eddy kinetic energy is spent to work against gravity, making the HETx configuration less efficient in transporting momentum and heat vertically than the HETy configuration.

Fluctuations of streamwise velocity, u_1', in an $x_1 - x_2$ plane just above the lower surface are shown in Fig. 19. Narrow streaks of large negative u_1' in simulation HET050y (right panel) immediately catch the eye (cf. low-momentum pathways considered in Bon and Meyers 2022). The streaks are locked to the surface temperature maxima, i.e., they are at the same spanwise positions as large positive temperature fluctuations (Fig. 17, right panel). Spatial correlations of u_1' and θ' results in the streaks of negative streamwise temperature flux shown in Fig. 20, right panel. The instantaneous structure of the $u_1'\theta'$ field is complex, with quiescent areas where $u_1'\theta'$ is nearly zero, and a number of spots of sophisticated shape where $u_1'\theta'$ is large and positive. However, elongated coherent patterns (streaks) of large negative $u_1'\theta'$ are dominant. This feature explains a negative mean streamwise turbulent temperature flux near the lower boundary in the simulations with the spanwise heterogeneity (Fig. 14). Note that, by symmetry about the mid-plane $x_3 = 1/2$, positive u_1' are collocated with negative θ' near the upper boundary, leading to a negative mean streamwise temperature flux there.

In the flows with the streamwise heterogeneity, the situation is not straightforward. Elongated patterns of positive and negative u_1', whose spanwise and streamwise size is about 0.2 and $1.0 - 1.5$, respectively, are identified in Fig. 19, left panel. Positive u_1' fluctuations located slightly downstream of the surface temperature maxima dominate. However, their collocation with the patterns of (large) positive θ' shown in Fig. 16, right panel, is not immediately apparent. Spatial correlation of u_1' and θ' results in a very complex field of the

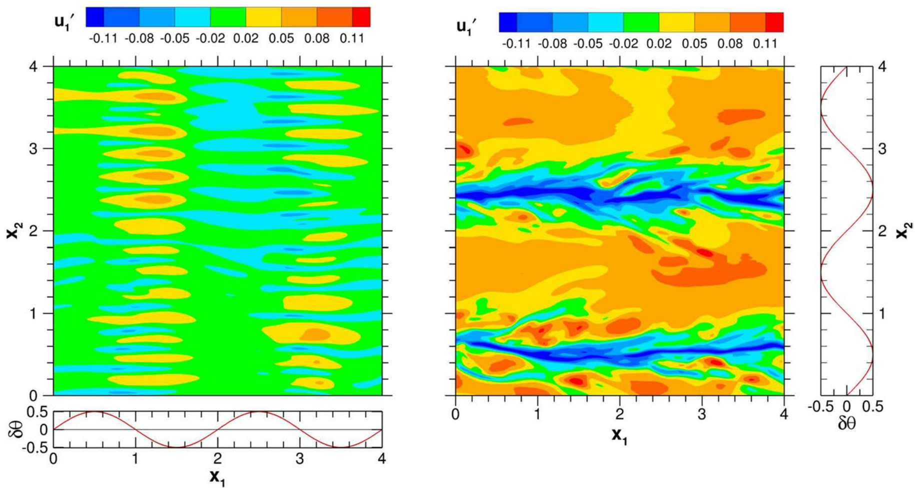

Fig. 19 Horizontal cross sections of the fluctuations of streamwise velocity about its horizontal mean value for simulations HET050x (left) and HET050y (right). Red (blue) colours correspond to positive (negative) values of u_1' as shown in the colour scale bars. The spatial variation of the imposed surface temperature θ_{sfc} is shown for each figure

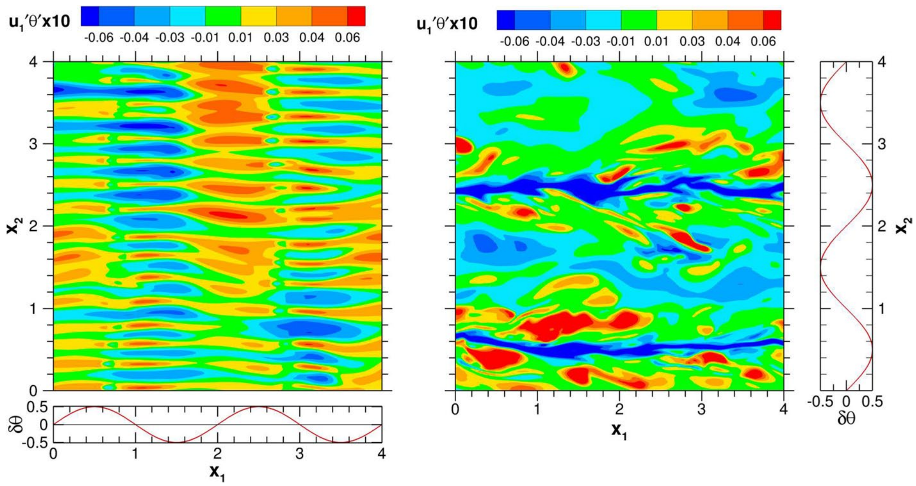

Fig. 20 Horizontal cross section of the streamwise temperature flux for simulations HET050x (left) and HET050y (right). Red (blue) colours correspond to positive (negative) values of the temperature flux (×10) as shown in the colour scale bars. The spatial variation of the imposed surface temperature θ_{sfc} is shown for each figure

streamwise turbulent temperature flux in the case HET050x (Fig. 20, left panel). The cross section is populated by elongated patterns of positive and negative $u_1'\theta'$ of various size and amplitude. Positive fluctuations dominate (albeit not strongly), leading to a positive mean streamwise turbulent temperature flux near the boundary in HETx simulations (Fig. 14).

Figure 21 further illustrates the difference between the flows with the streamwise and spanwise heterogeneity. In HET050y (right panel), large coherent patterns are readily identified. They extend from the walls towards the flow interior and nearly reach the mid-plane

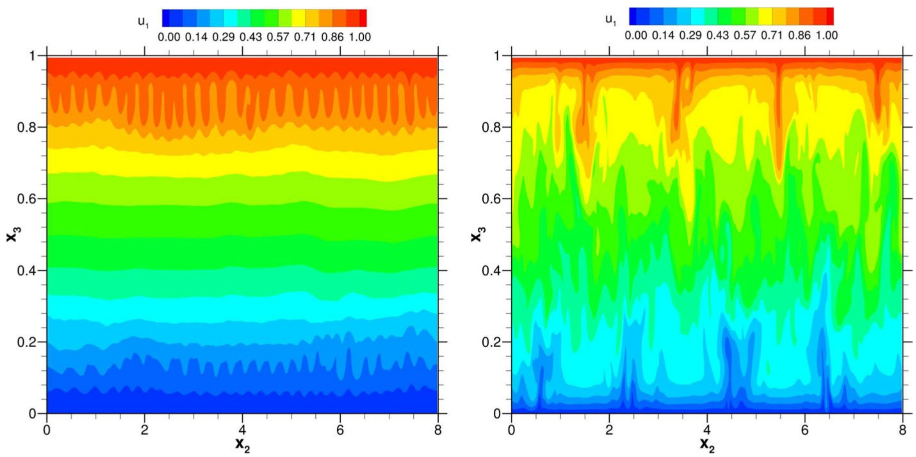

Fig. 21 Vertical $x_2 - x_3$ cross section of the streamwise velocity from simulations HET050x (left) and HET050y (right). The cross section is taken in the middle of the flow domain ($x_1 = 4$)

of the flow domain. Patterns of reduced streamwise velocity u_1 relative to the horizontal-mean $\overline{u}_1$ (low-momentum pathways) are located above the lower-wall temperature maxima, and patterns of enhanced u_1 (high-momentum pathways) are located below the upper-wall temperature minima. Both low-momentum pathways ($u' < 0$ and $w' > 0$) and high-momentum pathways ($u' > 0$ and $w' < 0$) make a remarkable contribution to the vertical flux of streamwise momentum that is down the gradient of mean streamwise velocity (Fig. 12). Generally, the case HET050y with the spanwise surface heterogeneity is characterized by high eddy activity in the entire flow domain. This is different in the HET050x case with the streamwise heterogeneity. Patterns with reduced/enhanced streamwise velocity are seen in Fig. 21(left), but those patterns have much smaller spatial scales and are not as exposed as in HET050y. Furthermore, a large part of the flow domain away from the walls is very quiet in terms of eddy activity.

5 Implications for Turbulence Closure Modelling

The differences between the flows with streamwise and spanwise surface thermal heterogeneity discussed in the previous sections have important implications for turbulence modelling of environmental and industrial flows within the RANS (Reynolds-Averaged Navier–Stokes) turbulence closure framework. Consider, for example, the effect of the streamwise temperature flux. A one-dimensional (the flow variables depend on the x_3 vertical co-ordinate only) RANS equation for the $\langle u_1' u_3' \rangle$ Reynolds-stress component (vertical flux of streamwise momentum) reads

$$\left(\frac{\partial}{\partial t} + \langle u_3 \rangle \frac{\partial}{\partial x_3}\right)\langle u_1' u_3' \rangle = -\left(\langle u_1' u_3' \rangle \frac{\partial \langle u_3 \rangle}{\partial x_3} + \langle u_3'^2 \rangle \frac{\partial \langle u_1 \rangle}{\partial x_3}\right) + g_3 \alpha_T \langle u_1' \theta' \rangle - \frac{\partial}{\partial x_3}\left(\langle u_1' u_3'^2 \rangle + \langle u_1' p' \rangle\right) - \epsilon_{13} + \left\langle p' \left(\frac{\partial u_1'}{\partial x_3} + \frac{\partial u_3'}{\partial x_1}\right)\right\rangle, \tag{15}$$

where ϵ_{13} is the dissipation rate of $\langle u_1' u_3' \rangle$. As different from the rest of the paper, the angle brackets in Eqs. (15) and (16) denote the Reynolds-mean quantities, and a prime denotes turbulent fluctuations. Recall that the x_3 vertical axis is aligned with the gravity vector and is positive upward. To simplify the discussion, we ignore the effect of the reference frame rotation on the second-order turbulence moments. As readily seen from Eq. (15), a negative $\langle u_1' \theta' \rangle$ (as in the HETy cases) contributes to the production of (negative) $\langle u_1' u_3' \rangle$, whereas a positive $\langle u_1' \theta' \rangle$ (as in the HETx cases) reduces the magnitude of $\langle u_1' u_3' \rangle$. Note in passing that the term with $\langle u_1' \theta' \rangle$ in Eq. (15) would be partially offset by a similar term that comes from the rapid part of the pressure-scrambling term, the last term on the r.h.s. of Eq. (15).

A one-dimensional RANS equation for the vertical turbulent temperature flux reads

$$\left(\frac{\partial}{\partial t} + \langle u_3 \rangle \frac{\partial}{\partial x_3}\right)\langle u_3' \theta' \rangle = -\langle u_3'^2 \rangle \frac{\partial \langle \theta \rangle}{\partial x_3} - \langle u_3' \theta' \rangle \frac{\partial \langle u_3 \rangle}{\partial x_3} + g_3 \alpha_T \langle \theta'^2 \rangle - \frac{\partial}{\partial x_3}\langle u_3'^2 \theta' \rangle - \epsilon_{\theta 3} - \left\langle \theta' \frac{\partial p'}{\partial x_3} \right\rangle, \tag{16}$$

where $\epsilon_{\theta 3}$ is the dissipation rate of $\langle u_3' \theta' \rangle$. The effect of the streamwise temperature flux $\langle u_1' \theta' \rangle$ on the vertical temperature flux $\langle u_3' \theta' \rangle$ is not readily seen from Eq. (16). The effect is hidden in the rapid contributions to the pressure-scrambling term, the last term on the r.h.s. of Eq. (16). Consideration of that and the associated effects is beyond the scope of the present paper. A physically sound turbulence closure model that accounts for the effect of the surface thermal heterogeneity, including the orientation of the heterogeneity patterns, is still to be developed. This should be a subject of future work.

6 Conclusions

Direct numerical simulations of plane Couette flows over thermally heterogeneous surfaces at bulk Reynolds number $Re = 10^4$ and bulk Richardson number $Ri = 0.25$ are performed. An idealized plane Couette flow configuration is used as a proxy for real-world stably-stratified environmental and industrial flows. The flow is driven by a constant velocity at the upper surface, while the lower surface is at rest. The temperature of the upper and lower walls is either homogeneous or varies sinusoidally, where the temperature-wave crests are either normal or parallel to the mean flow (HETx and HETy cases, respectively). Importantly, the horizontal-mean surface temperature is the same in all simulations. The focus of the present study that extends previous studies by the authors (Mironov and Sullivan 2016, 2023) is on the effect of the orientation of the surface heterogeneity patterns (relative to the mean velocity) on the boundary-layer structure and turbulence transport properties. To this end, DNS data are used to perform a comparative analysis of mean fields, second-order turbulence moments, vertical-velocity and temperature skewness, and the flow eddy structure in simulations with the streamwise and spanwise surface heterogeneity.

The buoyancy stratification at $Ri = 0.25$ is strong enough to fully quench turbulence over a homogeneous surface, although we give turbulence a good chance to survive by initializing the homogeneous simulation with a fully turbulent neutral Couette flow. However, turbulence survives over heterogeneous surfaces.

In all heterogeneous cases, both turbulence and molecular diffusion transport momentum down the gradient of the mean velocity. An outstanding feature of the heterogeneous simulations is the sign of the turbulent contribution to the vertical temperature (heat) flux near the upper and lower boundaries. The turbulent flux proves to be positive (upward), although the flow is stably stratified in the mean and the total (molecular plus turbulent) vertical temperature flux is down the gradient of the mean temperature (downward). Consideration of the vertical-velocity and temperature skewness suggests an analogy to convective boundary-layer flows, where counter-gradient heat transport is often encountered and is attributed to quasi-organized eddy structures (e.g., convective plumes and rolls) whose spatial scale is large as compared to the scale of chaotic, nearly isotropic turbulent motions. An examination of eddy structure of our heterogeneous Couette flows reveals that quasi-organized coherent eddy structures are indeed generated by the surface thermal heterogeneity. It is these structures that are responsible for turbulent transfer of heat up the gradient of the mean temperature.

A juxtaposition of HETx and HETy cases shows that the configuration with the spanwise heterogeneity is more turbulent and more efficient in transporting momentum and heat vertically than its counterpart with the streamwise heterogeneity. An analysis of the flow structure in the HETx and HETy cases suggests a physically plausible explanation of the difference between the two configurations revealed by the DNS (see sect. 4.6).

There is a striking difference between the HETx and HETy cases in terms of the streamwise temperature flux. In HETx cases, $u\theta$ is nearly zero in the middle of the flow domain and has pronounced maxima close to the upper and lower walls. In HETy cases, $u\theta$ is zero to positive in the middle of the domain and has pronounced minima close to the walls. That is, the streamwise heat flux differs not only in magnitude but also in sign. Visualization of the flow structure in sect. 4.6 helps explain the above difference.

The differences between the flows with streamwise and spanwise surface thermal heterogeneity have important implications for modelling turbulence in stably-stratified environmental and industrial flows within the RANS closure framework. Some implications are briefly discussed in sect. 5.

Future work should include a DNS/LES based comprehensive analysis of the second-moment budgets with the emphasis on the pressure-scrambling effects and the turbulence anisotropy. Furthermore, it remains to be seen if major conclusions from the present analysis (and the analysis of MS23) remain in force for other flow types, e.g., for pressure-gradient driven geophysical and industrial flows over homogeneous and heterogeneous surfaces. The present study has only addressed two configurations of the surface heterogeneity patterns, viz., the surface temperature waves normal and parallel to the mean flow. Analysis of other configurations is important, particularly in terms of the applicability of the DNS findings to real-world flows. For example, a checkerboard configuration and a configuration with randomly distributed warm and cold patches of different shapes are of interest for modelling atmospheric stably-stratified flows (cf. the channel flows with finite-length surface temperature strips analyzed by Bon et al. 2023).

Acknowledgements Thanks are due to Thijs Bon, Florian Prill, and Roland Wirth for discussions and helpful suggestions. The present study, which is an extension of the previous study by the authors (Mironov and Sullivan 2023), makes use of the DNS data from simulations HOM, HET025x, and HET50x reported in MS23. A description of governing equations, flow parameters, boundary conditions, and simulated cases in sects. 2 and 3 is to some extent similar to that in MS23. It is repeated here deliberately to make the present paper self-contained and ease the comprehension of material. Figure 16 and its description in sect. 4.6, and the left panel of Fig. 18 are adopted from MS23. The paper by Mironov and Sullivan (2023) is licensed under the Creative Commons Attribution 4.0 International License (https://creativecommons.org/licenses/by/4.0/).

Author Contributions The authors made equal contributions to the preparation of the manuscript.

Funding Open Access funding enabled and organized by Projekt DEAL.

Data Availibility Results from the DNS data analysis (vertical profiles and two-dimensional snapshots used for visualization, but not three-dimensional fields) can be obtained from the authors upon a reasonable request.

Declarations

Conflict of interest The authors declare that they have no conflict of interest.

Ethical approval Not applicable.

References

Alcántara-Ávila, F., Gandía-Barberá, S., Hoyas, S.: Evidences of persisting thermal structures in Couette flows. Int. J. Heat Fluid Flow **76**, 287–295 (2019). https://doi.org/10.1016/j.ijheatfluidflow.2019.03.001

Avsarkisov, V., Hoyas, S., Oberlack, M., et al.: Turbulent plane Couette flow at moderately high Reynolds number. J. Fluid Mech. **751**, R1 (2014). https://doi.org/10.1017/jfm.2014.323

Bon, T., Meyers, J.: Stable channel flow with spanwise heterogeneous surface temperature. J. Fluid Mech. **933**, A57 (2022). https://doi.org/10.1017/jfm.2021.1113

Bon, T., Broos, D., Cal, R.B., et al.: Secondary flows induced by two-dimensional surface temperature heterogeneity in stably stratified channel flow. J. Fluid Mech. **970**, A20 (2023). https://doi.org/10.1017/jfm.2023.619

Boyko, V., Vercauteren, N.: A stochastic stability equation for unsteady turbulence in the stable boundary layer. Quart. J. Roy. Meteorol. Soc. **149**, 2125–2145 (2023). https://doi.org/10.1002/qj.4498

Calaf, M., Vercauteren, N., Katul, G.G., et al.: Boundary-layer processes hindering contemporary numerical weather prediction models. Bound. Layer Meteorol. **186**, 43–68 (2023). https://doi.org/10.1007/s10546-022-00742-5

Chung, D., Matheou, G.: Direct numerical simulation of stationary homogeneous stratified sheared turbulence. J. Fluid Mech. **696**, 434–467 (2012)

Deusebio, E., Caulfield, C.P., Taylor, J.R.: The intermittency boundary in stratifid plane Couette flow. J. Fluid Mech. **781**, 298–329 (2015). https://doi.org/10.1017/jfm.2015.497

Gandía-Barberá, S., Alcántara-Ávila, F., Hoyas, S., et al.: Stratification effect on extreme-scale rolls in plane Couette flows. Phys. Rev. Fluids **6**, 034605 (2021). https://doi.org/10.1103/PhysRevFluids.6.034605

García-Villalba, M., Azagra, E., Uhlmann, M.: A numerical study of turbulent stably-stratified plane Couette flow. In: Nagel, W.E., Kröner, D.B., Resch, M.M. (eds.) Transactions of the High Performance Computing Center, Stuttgart, pp. 251–261. Springer, New York (2011)

Glazunov, A.V., Mortikov, E.V., Barskov, K.V., et al.: The layered structure of stably stratified turbulent shear flows. Izv. Atmos. Ocean. Phys. **55**, 312–323 (2019)

Holtslag, A.A.M., Svensson, G., Baas, P., et al.: Stable atmospheric boundary layers and diurnal cycles challenges for weather and climate models. Bull. Am. Meteorol. Soc. **94**, 1691–1706 (2013)

Jiménez, J.: Coherent structures in wall-bounded turbulence. J. Fluid Mech. **842**, P1 (2018). https://doi.org/10.1017/jfm.2018.144

Komminaho, J., Lundbladh, A., Johansson, A.V.: Very large structures in plane turbulent Couette flow. J. Fluid Mech. **320**, 259–285 (1996)

Lee, M.J., Kim, J.: The structure of turbulence in a simulated plane Couette flow. In: Proc. 8th Symposium on Turbulent Shear Flows. Technical Univ. of Munich, Munich, pp 5.3.1–5.3.6 (1991)

Lee, M., Moser, R.D.: Extreme-scale motions in turbulent plane Couette flows. J. Fluid Mech. **842**, 128–145 (2018). https://doi.org/10.1017/jfm.2018.131

Lenschow, D.H., Lothon, M., Mayor, S.D., et al.: A comparison of higher-order vertical velocity moments in the convective boundary layer from lidar with in situ measurements and LES. Bound. Layer Meteorol. **143**, 107–123 (2012)

Mahrt, L.: Stably stratified atmospheric boundary layers. Ann. Rev. Fluid Mech. **46**, 23–45 (2014). https://doi.org/10.1146/annurev-fluid-010313-141354

Mironov, D.V., Sullivan, P.P.: Second-moment budgets and mixing intensity in the stably stratified atmospheric boundary layer over thermally heterogeneous surfaces. J. Atmos. Sci. **73**, 449–464 (2016). https://doi.org/10.1175/JAS-D-15-0075.1

Mironov, D.V., Sullivan, P.P.: Turbulence structure and mixing in strongly stable boundary-layer flows over thermally heterogeneous surfaces. Bound. Layer Meteorol. **187**, 371–393 (2023). https://doi.org/10.1007/s10546-022-00766-x

Monin, A.S., Obukhov, A.M.: Basic laws of turbulent mixing in the atmospheric surface layer. Trudy Geofiz. Inst. Akad. Nauk. SSSR **24**(151), 163–187 (1954)

Monin, A.S., Yaglom, A.M.: Statistical Fluid Mechanics, vol. 1. MIT Press, Cambridge, Massachusetts (1971)

Mortikov, E.V., Glazunov, A.V., Lykosov, V.N.: Numerical study of plane Couette flow: turbulence statistics and the structure of pressure-strain correlations. Russ. J. Numer. Anal. Math. Modell. **34**, 119–132 (2019)

Nieuwstadt, F.T.M.: The turbulent structure of the stable, nocturnal boundary layer. J. Atmos. Sci. **41**, 2202–2216 (1984)

Nieuwstadt, F.T.M.: Direct numerical simulation of stable channel flow at large stability. Bound. Layer Meteorol. **116**, 277–299 (2005)

Obukhov, A.M.: Turbulence in thermally nonhomogeneous atmosphere. Trudy Inst. Teor. Geofiz. Akad. Nauk. SSSR **1**, 95–115 (1954)

Papavassiliou, D.V., Hanratty, T.J.: Interpretation of large-scale structures observed in a turbulent plane Couette flow. Int. J. Heat Fluid Flow **18**, 55–69 (1997)

Pirozzoli, S., Bernardini, M., Orlandi, P.: Turbulence statistics in Couette flow at high Reynolds number. J. Fluid Mech. **758**, 327–343 (2014). https://doi.org/10.1017/jfm.2014.529

Pope, S.B.: Turbulent Flows. Cambridge University Press (2000)

Richter, D.H., Sullivan, P.P.: Modification of near-wall coherent structures by inertial particles. Phys. Fluids **26**, 103304 (2014)

Stoll, R., Porté-Agel, F.: Surface heterogeneity effects on regional-scale fluxes in stable boundary layers: surface temperature transitions. J. Atmos. Sci. **66**, 412–431 (2009)

Stroh, A., Schäfer, K., Forooghi, P., et al.: Secondary flow and heat transfer in turbulent flow over streamwise ridges. Int. J. Heat Fluid Flow **81**, 108518 (2020). https://doi.org/10.1016/j.ijheatfluidflow.2019.108518

Sullivan, P.P., McWilliams, J.C.: Turbulent flow over water waves in the presence of stratification. Phys. Fluids **14**, 1182–1195 (2002)

Sullivan, P.P., Patton, E.G.: The effect of mesh resolution on convective boundary layer statistics and structures generated by large-eddy simulation. J. Atmos. Sci. **68**, 2395–2415 (2011)

Sullivan, P.P., McWilliams, J.C., Moeng, C.H.: Simulation of turbulent flow over idealized water waves. J. Fluid Mech. **404**, 47–85 (2000)

Sullivan, P.P., Weil, J.C., Patton, E.G., et al.: Turbulent winds and temperature fronts in large-eddy simulations of the stable atmospheric boundary layer. J. Atmos. Sci. **73**, 1815–1840 (2016)

Sullivan, P.P., McWilliams, J.C., Weil, J.C., et al.: Marine boundary layers above heterogeneous SST: across-front winds. J. Atmos. Sci. **77**, 4251–4275 (2020). https://doi.org/10.1175/JAS-D-20-0062.1

Sullivan, P.P., McWilliams, J.C., Weil, J.C., et al.: Marine boundary layers above heterogeneous SST: along-front winds. J. Atmos. Sci. **78**, 3297–3315 (2021). https://doi.org/10.1175/JAS-D-21-0072.1

van Hooijdonk, I.G.S., Clercx, H.J.H., Ansorge, C., et al.: Parameters for the collapse of turbulence in the stratified plane Couette flow. J. Atmos. Sci. **75**, 3211–3231 (2018)

Zhou, Q., Taylor, J.R., Caulfield, C.P.: Self-similar mixing in stratified plane Couette flow for varying Prandtl number. J. Fluid Mech. **820**, 86–120 (2017). https://doi.org/10.1017/jfm.2017.200